Article

Analytical Approach for a Heat Transfer Process through Nanofluid over an Irregular Porous Radially Moving Sheet by Employing KKL Correlation with Magnetic and Radiation Effects: Applications to Thermal System

Umair Khan [1,2] , Aurang Zaib [3] , Anuar Ishak [1] , Iskandar Waini [4] , Zehba Raizah [5,*] and Ahmed M. Galal [6,7]

[1] Department of Mathematical Sciences, Faculty of Science and Technology, Universiti Kebangsaan Malaysia UKM, Bangi 43600, Malaysia; umairkhan@iba-suk.edu.pk (U.K.); anuar_mi@ukm.edu.my (A.I.)

[2] Department of Mathematics and Social Sciences, Sukkur IBA University, Sukkur 65200, Pakistan

[3] Department of Mathematical Sciences, Federal Urdu University of Arts, Science & Technology, Gulshan-e-Iqbal, Karachi 75300, Pakistan; aurangzaib@fuuast.edu.pk

[4] Fakulti Teknologi Kejuruteraan Mekanikal dan Pembuatan, Universiti Teknikal Malaysia Melaka, Hang Tuah Jaya, Durian Tunggal 76100, Malaysia; iskandarwaini@utem.edu.my

[5] Department of Mathematics, College of Science, King Khalid University, Abha 62529, Saudi Arabia

[6] Mechanical Engineering Department, College of Engineering, Prince Sattam Bin Abdulaziz University, Wadi Addawaser 11991, Saudi Arabia; ahm.mohamed@psau.edu.sa

[7] Production Engineering and Mechanical Design Department, Faculty of Engineering, Mansoura University, P.O. Box 35516, Mansoura 35516, Egypt

* Correspondence: zaalrazh@kku.edu.sa

Abstract: The aluminum nanoparticle is adequate for power grid wiring, such as the distribution of local power and the transmission of aerial power lines, because of its higher conductivity. This nanoparticle is also one of the most commonly used materials in applications in the electrical field. Thus, in this study, a radiative axisymmetric flow of Casson fluid, induced by water-based Al_2O_3 nanofluid by using the Koo–Kleinstreuer–Li (KKL) correlation, is investigated. The impact of the magnetic field is also taken into account. KKL correlation is utilized to compute the thermal conductivity and effective viscosity. Analytical double solutions are presented for the considered axisymmetric flow model after implementing the similarity technique to transmute the leading equations into ordinary differential equations. The obtained analytic forms were used to examine and discuss the velocity profile, the temperature distribution, reduced heat transfer, and coefficient of reduced skin friction. The analytic solutions indicate that the velocity profile decreases in the branch of the first solution and uplifts in the branch of the second solution due to the presence of an aluminum particle, whereas the dimensionless temperature enhances in both solutions. In addition, the Casson parameter increases the friction factor, as well as the heat transport rate.

Keywords: axisymmetric flow; nanofluid; magnetic field; radiation effect; KKL correlation; moving sheet

1. Introduction

Heat transfer, which is regarded as the most important factor in most industrial and mechanical applications, is hampered by the profoundly low thermal conductivity of regular fluids. Heat transfer has a wide range of industrial applications that deal with both decreasing and increasing temperatures. Regular fluids, such as oil and water, have low thermal conductivity, which is the primary cause of engineering device inadequacy. In addition, the physical phenomena and parameters that influence the characteristics of the fluid flow and heat transfer in thermal systems composed of moving surfaces and working with nanofluids must be understood for the performance of these systems. Additionally, the fluid flow features, along with heat transfer in thermal systems, spanning from the

automotive radiator to the nuclear reactor, must be analyzed to evaluate the performance of the system. Heat transfer can be improved to improve the thermal system performance. Steve Papell of NASA USA (NASA Washington D.C., United States, NASA Johnson Space Center) developed the term ferrofluids in 1963 to create an appropriate fluid for rocket fuel that could be drawn through an external magnetic field towards the pump inlet in a zero-gravity environment. Later on, Choi [1] utilized the nanofluid, which refers to a mixture formed by dispersing nanoparticles in a host fluid. He defined nanotechnology as heat transfer fluids that have better thermal properties than base fluids or regular fluids. Nanofluids are made up of small amounts of congested particles that are 100 nanometers or smaller in size. Hamad et al. [2] considered the viscous flow induced by nanofluid absorbed in a porous media. The impact of the convective condition on fluid flow and heat transport conveying nanofluid past a stretchable sheet was examined by Makinde and Aziz [3]. Rana and Bhargava [4] scrutinized the behavior of nanofluid flow subject to the elongating of a non-linear horizontal stretchable sheet. Pal and Mandal [5] examined the impact of VD (viscous dissipation) on radiative flow, conveying nanofluid past a stretchable/shrinking sheet saturated in a porous media. The variable temperature flux of nanofluid near a stagnation point through a thin horizontal needle was studied by Hayat et al. [6]. Eid [7] inspected the collective influence of the chemical reaction on mixed convective MHD (magnetohydrodynamics) flow encompassing a two-phase nanofluid model past an exponentially elongated sheet with heat generation. Zaib et al. [8] examined the effect of nanofluid on bio-convective flow past a heated wedge in a Darcy–Brinkman medium. The effect of a slip stimulus on axisymmetric fluid flowing past a shrinking cylinder induced by a water-based copper nanofluid with mixed convection was explored by Soomro et al. [9]. Khan et al. [10] scrutinized the concave and convex effects on radiative mixed convective flow through an erratic moving sheet induced by a hybrid nanofluid. Zaher et al. [11] examined the EOF (electro-osmotic forces) through the boundary layer flow induced by Williamson nanofluid with microorganisms in a non-Darcy medium. Gowda et al. [12] analyzed a 2D ferromagnetic flow of nanofluid induced by a magnetic dipole past an elastic flat sheet with the Stefan blowing condition. Recently, Shahid et al. [13] inspected the bi-convection flow induced by Carreau nanofluid past a paraboloid permeable upper surface with a chemical reaction and activation energy.

The rheological properties of non-Newtonian fluids sparked widespread curiosity due to their prospective applications in an extensive range of technological, industrial, and pharmaceutical applications, such as crystal manufacturing and the manufacture offiber equipment. Non-Newtonian fluids are classified into numerous types, which are labeled as integral form (a sort of intensity), and differential form, for a broader understanding. Foams, melts, polymer solutions, and suspensions are offered as common examples of the materials that, under the right conditions, exhibit shear-thickening, shear-thinning, time-dependent, viscoplastic, and viscoelastic behavior. The model of Casson fluid is widely used to explain non-Newtonian fluids and their behavior. Casson fluid is identified as a shear-thinning fluid. It is a compelling fluid model because of its significant valuable inferences in our daily lives, such as in the polymer processing and biomedical fields. It offers a great framework for analyzing the two features in practice, apparent yield stress and Cason viscosity. Mukhopadhyay et al. [14] explored the two-dimensional flow of Casson fluid past an irregular stretchable sheet. Nadeem et al. [15] and Pramanik [16] scrutinized the Casson fluid flow past exponentially shrinking and stretching sheets, respectively. Haq et al. [17] examined the Casson fluid flow through a shrinkable heated sheet and found double solutions. Makinde et al. [18] incorporated the consequence of the MHD field on Casson fluid flow past a thermally horizontal melting stratified surface. Faraz et al. [19] observed the Soret/Dufour effects and chemical reactions on unsteady axisymmetric flow induced by Casson fluid past a radially stretchable sheet with multi-slip effects. The impact of the Lorentz force on non-linear radiative flow via a Casson fluid from a stretchable rotating heated disc was inspected by Khan et al. [20]. Zaib et al. [21] investigated the slip impacts on Casson fluid flow past a vertical plate immersed in Darcy–Brinkman medium with mixed

convection and presented double solutions for slip parameters. Recently, Jyothi et al. [22] utilized the model of modified Buongiorno to investigate the effect of activation energy on the flow of Casson fluid induced by hybrid nanofluid past a downward/upward-moving rotatable disk.

Consideration of the radiation effect adds a novel dimension to boundary-layer flow (BLF) and heat transport. The effects of radiative heat transport on dissimilar flows are critical in processes of high temperature and space technology. Thermal radiation can have a significant impact on heat transport and distribution of temperature in the BLF of a participating liquid at high temperatures. In recent years, significant endeavors were composed to obtain a better grip on the cooling rate. Some significant applications of radiative heat transfer include high-temperature plasmas, liquid metal fluids, cooling of a nuclear reactor, and systems of power generation. Several authors [23–27] studied distinct problems by considering the radiation effect on heat transfer. Daniel et al. [28] investigated unsteady radiative flow via a stretched sheet induced by nanofluid with the MHD field. Mekheimer et al. [29] inspected the influence of a chemical reaction on the radiative flow through Prandtl fluid with microorganisms past a porous, stretchable/shrinkable sheet. The impacts of radiation and melting on magneto Casson fluid via a porous, stretchable sheet with a chemical reaction were inspected numerically by Ramana et al. [30]. Abbas et al. [31] studied the impact of radiation on the squeezed flow through the suspension of particle fluid between parallel plates with oscillations. Lately, Khan et al. [32] discussed the radiation impact on blood flow induced by Casson fluid conveying gold particles through stretchable/shrinkable sheets with entropy generation.

The axisymmetric flow past a radially shrinking or stretching sheet has numerous manufacturing and industrial applications, including the production of glass fibers, mechanized plastic sheets and foods, polymer sheets, and coating for wires. According to a review of the literature, Arial [33] was the first to address axisymmetric flow over a linearly stretched sheet and to arrive at an exact and numerical solution. By using the variational iterative technique, Mirgolbabaei et al. [34] were able to provide an analytical solution to this problem. Ariel [35] expanded the axisymmetric flow problem to second-grade fluids. Sahoo [36] explored the role of partial slip on the magneto axisymmetric flow of viscoelastic fluid via a stretchable surface. Recently, Shahzad et al. [37] considered the axisymmetric flow through an exponential stretchable sheet with the magnetic field.

Based on the above literature reviews, it is apparent that, to the finest of the writer's awareness, there is a lot of research and modeling about nanofluid flow through various surfaces in the literature. However, there are no results/efforts conducted with regard to the 2D flow stream of nanofluid past a porous, radially shrinkable sheet induced by Casson fluid with radiation effects using the KKL model. Thus, in this exploration, exact solutions of Casson fluid are presented by employing the KKL model correlation induced by Al_2O_3 nanofluid past a porous, radially shrinking sheet with radiation effect. In addition, the fluctuations in the velocity and thermal gradients are graphically deliberated.

2. Mathematical Modeling
2.1. Constitutive Equation

The state of the rheological equation for Casson incompressible fluid is stated as [38,39]

$$\Gamma_{ij} = \begin{cases} 2\left(\mu_b + \frac{p_y}{\sqrt{2\pi}}\right)e_{ij}, \pi > \pi_c \\ 2\left(\mu_b + \frac{p_y}{\sqrt{2\pi}}\right)e_{ij}, \pi < \pi_c \end{cases}. \tag{1}$$

where, $\pi = e_{ij}e_{ij}$ and e_{ij} are the (i,j)th deformation rates' components, π is signified as the production of deformation rates' components with itself, π_c is presented as critical value and p_y, μ_b are identified as the yield stress and dynamic viscosity of the non-Newtonian fluid, respectively.

2.2. Basic Equations

In the considered problem, the radiative axisymmetric flow and heat transport simulated by the (water-Al$_2$O$_3$) Casson nanofluid are investigated from a continuously nonlinear, radially shrinking permeable sheet with variable wall temperature, comprising the correlation of the Koo–Kleinstreuer and Li (KKL) model. Therefore, the flow problem configuration is schematically revealed in Figure 1, where the Cartesian cylindrical coordinates (r_b, δ, z_b) are taken to be in such a way that the r_b-axis is considered parallel to the sheet and the z_b-axis is measured perpendicular to it, and the flow is occurring in the $(r_b, \delta)-$plane. The considered flow is symmetric as well as axisymmetric about the $(r_b, \delta)-$plane and z_b-axis, respectively. Meanwhile, the partial modification in all variables in relation to δ is going to be completely terminated, and mathematically, it is expressed as $\partial/\partial\delta = 0$. In addition, the surface velocity is presumed as $u_w(r_b) = cr_b{}^3$, where c signifies as an arbitrary constant. Moreover, the exterior magnetic field is considered in changeable form as $B(r_b) = r_b B_0$, which carries out normally to the sheet's surface (see Appendix A for derivation of the magnetic field). Furthermore, the sheet's surface is also assumed to be permeable, and the corresponding wall mass transfer velocity is captured as $w_w(r_b) = -r_b v_0$, with $w_w < 0$ and $v_0 > 0$ referring to mass blowing or injection, while $w_w > 0$ and $v_0 < 0$ denote a mass suction phenomenon, respectively. Additionally, the temperature is considered as $T_\infty < T_w$, where T_∞ and T_w designate the steady freestream temperature and the variable or power law wall temperature, respectively.
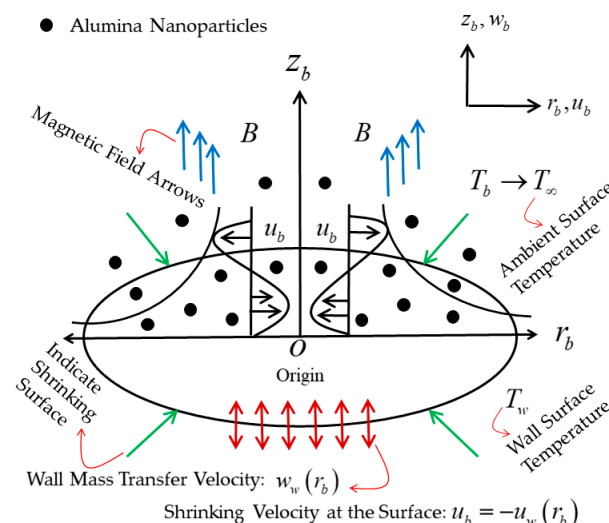

Figure 1. The physical model of the flow and coordinate system.

The properties of the aluminum oxide (Al$_2$O$_3$) nanoparticles and the base fluid (H$_2$O) are taken to be constant and no slip happens between them. The nanofluid thermophysical features are specified in Table 1. Under these postulations, the steady basic governing equations in the partial differential equations form are written as follows [40]:

$$\frac{\partial u_b}{\partial r_b} + \frac{u_b}{r_b} + \frac{\partial w_b}{\partial z_b} = 0, \tag{2}$$

$$u_b \frac{\partial u_b}{\partial r_b} + w_b \frac{\partial u_b}{\partial z_b} = \frac{\mu_{nf}}{\rho_{nf}}\left[\frac{(\chi+1)}{\chi}\right]\frac{\partial^2 u_b}{\partial z_b^2} - \sigma_{nf}\frac{B^2(r_b)}{\rho_{nf}}u_b, \tag{3}$$

$$u_b \frac{\partial T_b}{\partial r_b} + w_b \frac{\partial T_b}{\partial z_b} = \frac{k_{nf}}{(\rho c_p)_{nf}}\frac{\partial^2 T_b}{\partial z_b^2} - \frac{1}{(\rho c_p)_{nf}}\frac{\partial}{\partial z_b}(q_{rad}), \tag{4}$$

where w_b and u_b symbolize the velocity components in the respective direction of the z_b- and r_b-axes, respectively, T_b is the temperature of the fluid and χ is the non-Newtonian or Casson fluid parameter, while the other mathematical letters are recognized and determined

later for the nanofluid and KKL (Koo–Kleinstreuer and Li) model. The viscous dissipation (VD) term is ignored in the suggested equation of energy (4), whilst the radiative term of heat flux, q_{rad}, is appended through the Rosseland approximations in the easiest form as follows:

$$q_{rad} = \frac{-16\sigma_C T_\infty^3}{3k_C} \frac{\partial T_b}{\partial z_b} \tag{5}$$

Table 1. Thermophysical properties of the nanofluid.

Physical Properties	Water	Al$_2$O$_3$
k (Wm^{-1}K^{-1})	0.613	25
c_p (J kg^{-1} K^{-1})	4179	765
ρ (kg m^{-3})	997.1	3970
σ $(\Omega\mathrm{m})^{-1}$	0.05	1×10^{-10}
d_{pa} (nm)	-	47
Pr	6.2	-

Here, in the aforementioned Equation (5), σ_C and k_C delegate the constant of Stefan Boltzmann and the coefficient of mean absorption. For further simplicity, the Equation (4), together with Equation (5), can be preserved in a new compact form as:

$$u_b \frac{\partial T_b}{\partial r_b} + w_b \frac{\partial T_b}{\partial z_b} = \frac{k_f}{(\rho c_p)_{nf}} \left(\frac{k_{nf}}{k_f} + \frac{4}{3} R_d \right) \frac{\partial^2 T_b}{\partial z_b^2}, \tag{6}$$

where k_f represents the base fluid's electrical conductivity and $R_d = \frac{4\sigma_C T_\infty^3}{k_C k_f}$ represents the dimensionless radiation parameter. The BCs (boundary conditions) of the problem are:

$$\left. \begin{array}{c} u_b = -u_w(r_b), \ w_b = w_w(r_b), \ T_b = T_w \ \left(T_w = T_\infty + r_b^m T_0\right) \text{at } z_b = 0, \\ u_b \to 0, T_b \to T_\infty \text{ as } z_b \to \infty, \end{array} \right\} \tag{7}$$

where T_0 is the constant reference temperature, and m is the relative factor of the power law index. Furthermore, the rest of the mathematical notations in the governing equation are namely illustrated as $(\rho c_p)_{nf}$ the effective specific heat capacity at the constant pressure, σ_{nf} the effective electrical conductivity, and ρ_{nf} the effective density of the nanofluid, which is demarcated as (see [41,42]):

$$(\rho c_p)_{nf} = \phi(\rho c_p)_{pa} + (1-\phi)(\rho c_p)_f, \rho_{nf} = \phi \rho_{pa} + (1-\phi)\rho_f,$$
$$\sigma_{nf} = \left[1 + \frac{3(\sigma_{pa}/\sigma_f - 1)\phi}{(\sigma_{pa}/\sigma_f + 2) - (\sigma_{pa}/\sigma_f - 1)\phi} \right] \sigma_f, \tag{8}$$

where ϕ signifies the solid nanoparticle volume fraction. Additionally, $(\rho c_p)_f$, σ_f, and ρ_f are the respective quantities of the regular-based fluid. However, the subscripts in Equation (8) are the following: f, pa and nf, which reveal the regular-based fluid, nanoparticles, and nanofluid, respectively.

The Brownian motion has a substantial effect on the thermal conductivity, k_{nf}, of the nanofluid. Koo and Kleinstreuer [43] suggested that k_{nf} consists of the conventional static part of the particle and the Brownian part of the motion. The considered model of k_{nf} consists of two components that take the impacts of temperature dependence, the volume fraction of particle and particle size, and types of particle and fluid base groupings into account. Let us mathematically express it as [43]:

$$k_{nf} = k_{Brownian} + k_{static} \tag{9}$$

$$\frac{k_{static}}{k_f} = 1 + \frac{3\left(\frac{k_{pa}}{k_f} - 1\right)\phi}{\left(\frac{k_{pa}}{k_f} + 2\right) - \left(\frac{k_{pa}}{k_f} - 1\right)\phi} \tag{10}$$

where k_{static} signifies the Maxwell classical correlation-based static thermal conductivity. A simulation of the flow of Stokes around a sphere results in an enriched k_f, produced by a convective micro-size particle and a heat transfer of Brownian particle speed, affecting the far-field fluid movement (nanomaterials). Additionally, to the influence of temperature's role in the given model, the interaction between nanoparticles was combined by the introduction of two empirical functions (γ and h) Koo [44], which leads to:

$$k_{Brownian} = 5 \times 10^4 \gamma \phi \rho_f c_{p,f} \sqrt{\frac{\kappa_b T_b}{\rho_{pa} d_{pa}}} h(T_b, \phi) \tag{11}$$

The significance of the interfacial thermal resistance between base fluid and nanoparticles was emphasized progressively in recent years (see, Jang and Choi [45] and Prasher et al. [46]). In the nearby layers of two dissimilar types of material, such as the TIR, Kapitza resistance is alleged to be present; the thin barrier layer participates a crucial role in deteriorating the effective thermal conductivity of the nanoparticles. Li [47] reviewed the Koo and Kleinstreuer model [43] and combined γ and h functions to build up a new H function to capture the impacts of temperature, particle diameter, and nanoparticles on volume fraction. The empirical (H-function) of the nanofluid depends upon its type [48]. In addition, the original $\left(k_{pa}\right)$ in Equation (10) was changed by the new $\left(k_{pa,eff}\right)$ form (given below) with the introduction of the thermal interfacial resistance ($R_f = 4 \times 10^{-8}$ km^3/W):

$$R_f + \frac{d_{pa}}{k_{pa}} = \frac{d_{pa}}{k_{pa,eff}} \tag{12}$$

The function should be dissimilar for distinct nanoparticles and regular fluids. The current study only considers water-based nanofluids. For water-Al$_2$O$_3$ nanofluids, the following format should be read as follows:

$$H(T_b, \phi, d_{pa}) = \left(b_1 + b_2 \ln(d_{pa}) + b_5 \ln(d_{pa})^2 + b_3 \ln(\phi) + b_4 \ln(d_{pa})\ln(\phi)\right)\ln(T_b) +$$

$$\left(b_6 + b_7 \ln(d_{pa}) + b_{10} \ln(d_{pa})^2 + b_8 \ln(\phi) + b_9 \ln(d_{pa})\ln(\phi)\right),$$

$$\phi \le 0.04, \qquad 300K \le T_b \le 325K.$$

$$\tag{13}$$

The R^2 of water- Al$_2$O$_3$ nanofluid is 96% and 98%, respectively [48] (Table 2). The coefficients b_i ($i = 1\ldots10$) are based on the type of nanoparticles, and also on these coefficients. Finally, the correlation of KKL (Koo–Kleinstreuer–Li) is given by:

$$k_{Brownian} = 5 \times 10^4 \phi \rho_f c_{p,f} \sqrt{\frac{\kappa_b T_b}{\rho_{pa} d_{pa}}} H(T_b, \phi, d_{pa}) \tag{14}$$

Table 2. Constants of water-Al_2O_3 nanofluid.

Coefficient Values	Water-Al_2O_3
c_1	52.813
c_2	6.115
c_3	0.695
c_4	4.1×10^{-2}
c_5	0.176
c_6	$-2.98.198$
c_7	-34.532
c_8	-3.922
c_9	-0.235
c_{10}	-0.999

Koo and Kleinstreuer [43] examined the laminar nanofluid flow in micro-heat sinks using their efficient thermal conductivity model of nanofluid. Therefore, in regard to the absolute μ_{nf} (viscosity) owing to the suspension of micro-mixing, the proposed expression is stated as:

$$\mu_{nf} = \mu_{Brownian} + \mu_{static} = \mu_{static} + \frac{\mu_f k_{Brownian}}{\text{Pr}k_f} \qquad (15)$$

where $\mu_{static} = \frac{\mu_f}{(1-\phi)^{2.5}}$ represents a nanofluid static viscosity that Brinkman originally defines.

2.3. Non-Dimensional Equations

To facilitate the investigation of the problem, the appropriate self-similarity variables are proposed here:

$$\xi = \sqrt{\frac{c}{\nu_f}} z_b r_b, \theta(\xi) = \frac{T - T_\infty}{T_w - T_\infty}, \ \psi = -\sqrt{c\nu_f} r_b^3 G(\xi) \qquad (16)$$

where ν_f is the kinematic viscosity and ψ is the stream function. Next, employ the description of ψ in component form as $u_b = \frac{1}{r_b} \frac{\partial \psi}{\partial z_b}$ and $w_b = -\frac{1}{r_b} \frac{\partial \psi}{\partial r_b}$. Now, utilize Equation (16) in these given equations to acquire the velocities in the following form:

$$u_b = c r_b^3 G'(\xi) \ \text{and} \ w_b = -\sqrt{c\nu_f} \, r_b \big(3G(\xi) + \xi G'(\xi)\big) \qquad (17)$$

Thus, the similarity transformation and, the equation of continuity is held, whilst the leading Equations (3) and (6), along with the BCs (7), are eased to the dimensional form of ODEs as follows:

$$\frac{\mu_{nf}/\mu_f}{\rho_{nf}/\rho_f} \left[\frac{(\chi+1)}{\chi} \right] G''' + 3GG'' - 3G'^2 - \frac{\sigma_{nf}/\sigma_f}{\rho_{nf}/\rho_f} M_b G' = 0, \qquad (18)$$

$$\frac{1}{\text{Pr}(\rho c_p)_{nf}/(\rho c_p)_f} \left(k_{nf}/k_f + \frac{4}{3} R_d \right) \theta'' + 3G\theta' - m\theta G' = 0, \qquad (19)$$

subject to the following BCs:

$$\left. \begin{array}{l} G'(\xi) = -1, G(\xi) = S_b, \ \theta(\xi) = 1 \ \text{at} \ \xi = 0 \\ G'(\xi) \to 0, \ \theta(\xi) \to 0 \ \text{as} \ \xi \to \infty \end{array} \right\} \qquad (20)$$

where primes ($'$) exemplify the differentiation w.r.t ξ. The dimensionless constants involved in the problem are the magnetic parameter M_b and the mass transfer factor S_b, with $S_b > 0$ for suction and $S_b < 0$ for injection, posited mathematically as follows:

$$M_b = \frac{\sigma_f B_0^2}{\rho_f c}, S_b = \frac{v_0}{3\sqrt{cv_f}} \tag{21}$$

2.4. Gradients

The wall drag force or shear stress C_g and heat transfer Nu_{r_b} are important gradients for engineering physical quantities of attention that are used for the behavior of the fluid flow dynamics, as well as the local heat transfer characteristics. These gradients are mathematically defined as

$$C_g = \frac{2\mu_{nf}}{\rho_f u_w^2}\left(\frac{\partial u_b}{\partial z_b}\right)\bigg|_{z_b=0}, \qquad Nu_{r_b} = -\frac{r_b k_{nf}}{k_f(T_w - T_\infty)}\left(\frac{\partial T_b}{\partial z_b}\right)\bigg|_{z_b=0}. \tag{22}$$

Replacing Equation (16) into the aforementioned Equation (22), we find the required reduced form of the wall drag force and heat transfer, which can take place as follows:

$$\frac{1}{2}\mathrm{Re}_{r_b}^{1/2} C_g = \frac{\mu_{nf}}{\mu_f} G''(0), \qquad \mathrm{Re}_{r_b}^{-1/2} Nu_{r_b} = -\frac{k_{nf}}{k_f}\theta'(0), \tag{23}$$

where $\mathrm{Re}_{r_b} = \frac{u_w(r_b)r_b}{v_f}$ signifies the Reynolds number.

3. Analytic Solutions Methodology

This section of the paper illustrates how the analytical solution technique works. In this considered problem, we must determine the closed-form precise solutions to Equations (18) and (19) subject to the required BCs (20). Therefore, keeping the comparable previous papers approach in mind [49–51], we acquire the analytical or exact solution of Equation (18), subject to BCs (20) in the following form:

$$G(\xi) = S_b - \frac{1}{D}\left(1 - e^{-D\xi}\right). \tag{24}$$

Plugging Equation (24) for dimensionless similarity in Equation (18) yields the following second-order algebraic equation, which may be interpreted as:

$$\frac{\mu_{nf}}{\mu_f}\left[\frac{(\chi+1)}{\chi}\right]D^2 - 3S_b\frac{\rho_{nf}}{\rho_f}D + 3\frac{\rho_{nf}}{\rho_f} - \frac{\sigma_{nf}}{\sigma_f}M_b = 0 \tag{25}$$

where

$$D = \frac{3S_b\left(\rho_{nf}/\rho_f\right) \pm \sqrt{9S_b^2\left(\rho_{nf}/\rho_f\right)^2 - 4\left(\mu_{nf}/\mu_f\right)\left[\frac{(\chi+1)}{\chi}\right]\left(3\left(\rho_{nf}/\rho_f\right) - \left(\sigma_{nf}/\sigma_f\right)M_b\right)}}{2\left(\mu_{nf}/\mu_f\right)\left[\frac{(\chi+1)}{\chi}\right]}$$

Furthermore, the suggested problem has upper and lower branch solutions (dual or multiple solutions), as evidenced by the two distinct roots mentioned above. Additionally, Equation (24) depicts the velocity $G'(\xi)$ and shear stress $G''(\xi)$ at the wall surface, which are given by:

$$G'(\xi) = -e^{-D\xi} \tag{26}$$

and

$$G''(0) = \frac{3S_b\left(\rho_{nf}/\rho_f\right) \pm \sqrt{9S_b^2\left(\rho_{nf}/\rho_f\right)^2 - 4\left(\mu_{nf}/\mu_f\right)\left[\frac{(\chi+1)}{\chi}\right]\left(3\left(\rho_{nf}/\rho_f\right) - \left(\sigma_{nf}/\sigma_f\right)M_b\right)}}{2\left(\mu_{nf}/\mu_f\right)\left[\frac{(\chi+1)}{\chi}\right]} \tag{27}$$

To decipher Equation (19) exactly with the BC (20), we require the solution of Equation (24) in the realizable energy equation to catch the requisite form as follows:

$$\theta'' + \frac{3\mathrm{Pr}(\rho c_p)_{nf}/(\rho c_p)_f}{\left(\frac{k_{nf}}{k_f} + \frac{4}{3}R_d\right)}\left(S_b - \frac{1}{D} + \frac{1}{D}e^{-D\xi}\right)\theta' + \frac{m\mathrm{Pr}(\rho c_p)_{nf}/(\rho c_p)_f}{\left(\frac{k_{nf}}{k_f} + \frac{4}{3}R_d\right)}\theta e^{-D\xi} = 0 \tag{28}$$

Here, we suppose a new variable $\eta = \frac{3\mathrm{Pr}(\rho c_p)_{nf}/(\rho c_p)_f}{(k_{nf}/k_f + \frac{4}{3}R_d)D^2}e^{-D\xi}$ for Equation (28) to find their closed-form analytical solution. Therefore, implementing a new variable in the Equation (28) and the border ailment (20) yields:

$$\eta\frac{d^2\theta}{d\eta^2} + (L - \eta)\frac{d\theta}{d\eta} - P\theta = 0, \tag{29}$$

where $L = 1 - \frac{3\mathrm{Pr}(\rho c_p)_{nf}/(\rho c_p)_f}{\left(\frac{k_{nf}}{k_f} + \frac{4}{3}R_d\right)D}\left(S_b - \frac{1}{D}\right)$ and $P = -\frac{m}{3}$.

In terms of a new variable, the subject BCs are:

$$\theta\left(\frac{3\mathrm{Pr}(\rho c_p)_{nf}/(\rho c_p)_f}{\left(\frac{k_{nf}}{k_f} + \frac{4}{3}R_d\right)D^2}\right) = 1 \quad \text{and} \quad \theta(0) = 0 \tag{30}$$

Thus, the general solution for Equation (29) is given as:

$$\theta(\eta) = B_1 M(P, L, \eta) + B_2\eta^{1-L}M(P + 1 - L, 2 - L, \eta) \tag{31}$$

where M is the first kind of confluent hypergeometric function or Kummer function with B_1 and B_2 being arbitrary constants.

Using the values of L and P along with BCs (30) in the general solution of Equation (31), we get:

$$\theta(\eta) = \frac{\left(\frac{\eta\left(k_{nf}/k_f + \frac{4}{3}R_d\right)D^2}{3\mathrm{Pr}(\rho c_p)_{nf}/(\rho c_p)_f}\right)^{D_b}M\left(D_b - \frac{m}{3}, 1 + D_b, \eta\right)}{M\left(D_b - \frac{m}{3}, 1 + D_b, \frac{3\mathrm{Pr}(\rho c_p)_{nf}/(\rho c_p)_f}{\left(k_{nf}/k_f + \frac{4}{3}R_d\right)D^2}\right)} \tag{32}$$

$$D_b = \frac{3\mathrm{Pr}(\rho c_p)_{nf}/(\rho c_p)_f}{\left(k_{nf}/k_f + \frac{4}{3}R_d\right)D}\left(S_b - \frac{1}{D}\right)$$

Thus, the analytical solution of the temperature, in terms of ξ, is given by as:

$$\theta(\xi) = \frac{e^{-DD_b\xi}M\left(D_b - \frac{m}{3}, 1 + D_b, \frac{3\mathrm{Pr}(\rho c_p)_{nf}/(\rho c_p)_f}{(k_{nf}/k_f + \frac{4}{3}R_d)D^2}e^{-D\xi}\right)}{M\left(D_b - \frac{m}{3}, 1 + D_b, \frac{3\mathrm{Pr}(\rho c_p)_{nf}/(\rho c_p)_f}{(k_{nf}/k_f + \frac{4}{3}R_d)D^2}\right)} \tag{33}$$

Now captivating the first derivative of Equation (32) w.r.t ξ, it becomes

$$
\theta'(\xi) = -\frac{DD_b e^{-DD_b\xi} M\left(D_b - \frac{m}{3}, 1+D_b, \frac{3\mathrm{Pr}(\rho c_p)_{nf}/(\rho c_p)_f}{\left(k_{nf}/k_f + \frac{4}{3}R_d\right)D^2} e^{-D\xi}\right)}{M\left(D_b - \frac{m}{3}, 1+D_b, \frac{3\mathrm{Pr}(\rho c_p)_{nf}/(\rho c_p)_f}{\left(k_{nf}/k_f + \frac{4}{3}R_d\right)D^2}\right)}
$$

$$
-\frac{3\left(D_b - \frac{m}{3}\right)e^{-D\xi - D_b D\xi}\mathrm{Pr}(\rho c_p)_{nf}/(\rho c_p)_f M\left(D_b - \frac{m}{3} + 1, 2+D_b, \frac{3\mathrm{Pr}(\rho c_p)_{nf}/(\rho c_p)_f}{\left(k_{nf}/k_f + \frac{4}{3}R_d\right)D^2} e^{-D\xi}\right)}{\left(k_{nf}/k_f + \frac{4}{3}R_d\right)D(1+D_b)M\left(D_b - \frac{m}{3}, 1+D_b, \frac{3\mathrm{Pr}(\rho c_p)_{nf}/(\rho c_p)_f}{\left(k_{nf}/k_f + \frac{4}{3}R_d\right)D^2}\right)}.
$$

(34)

The heat transfer rate at the wall is specified as

$$
-\theta'(0) = DD_b + \frac{3\left(D_b - \frac{m}{3}\right)\mathrm{Pr}(\rho c_p)_{nf}/(\rho c_p)_f M\left(D_b - \frac{m}{3} + 1, 2 + D_b, \frac{3\mathrm{Pr}(\rho c_p)_{nf}/(\rho c_p)_f}{\left(k_{nf}/k_f + \frac{4}{3}R_d\right)D^2}\right)}{\left(k_{nf}/k_f + \frac{4}{3}R_d\right)D(1+D_b)M\left(D_b - \frac{m}{3}, 1+D_b, \frac{3\mathrm{Pr}(\rho c_p)_{nf}/(\rho c_p)_f}{\left(k_{nf}/k_f + \frac{4}{3}R_d\right)D^2}\right)}.
$$

(35)

4. Results and Discussion

In this proposed portion, we essentially demonstrated, geometrically discussed, and physically interpreted the closed-form analytical solutions of the current water-Al_2O_3 nanofluid problem for the two distinct solution branches (first and second solutions), which may be shown visually in Figures 2–13. In these prepared various distinct plots, we displayed the graphical behavior of the velocity profiles, temperature distribution, heat transfer, and wall drag force with the influence of various distinct factors, such as radiation parameter R_d, solid nanoparticle volume fractions ϕ, magnetic parameter M_b, mass suction parameter S_b, and non-Newtonian or Casson fluid parameter χ. The problem exhibited two distinct branch solutions (first and second), where the first branch solution in the entire paper is accessible by the solid red lines, and the second branch solution is revealed by the solid green lines. Moreover, the thermophysical properties of the aluminum oxide (Al_2O_3) nanoparticles and the base fluid (H_2O) are arranged in Table 1, while the values of their constants of the water-Al_2O_3 nanofluid are written in Table 2. Tables 3 and 4 are prepared to examine the suction effect on wall drag force and heat transfer. Table 3 indicates that the value of $\left(\mu_{nf}/\mu_f\right)G''(0)$ increases for the outcome of the first branch and declines for the outcome of the second branch. This trend may imply a flow with separation. This trend may imply a flow with separation, in which the structure of a tiny wake may minimize the wall drag force past a shrinkable sheet. Thus, the values of $\left(\mu_{nf}/\mu_f\right)G''(0)$ decline.

Table 4 suggests the values of $-\left(k_{nf}/k_f\right)\theta'(0)$ augmenting due to greater intensity of suction in both branches of the solution. Physically, as the suction uplifts, it enhances the porosity of the sheet, which ultimately permits more nanoparticles to disperse the sheet. As a consequence, the rate of heat transfer is augmented as suction enhances.
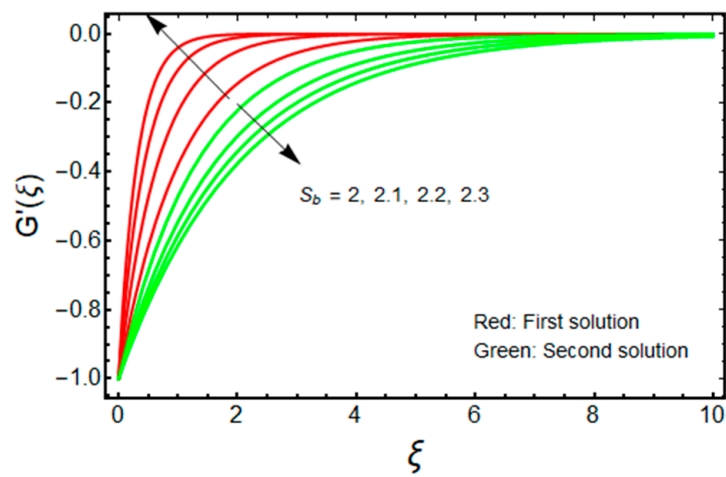
Figure 2. Effect of S_b on $G'(\xi)$ when $\phi = 0.025$, $\chi = 1$, $M_b = 0.5$.
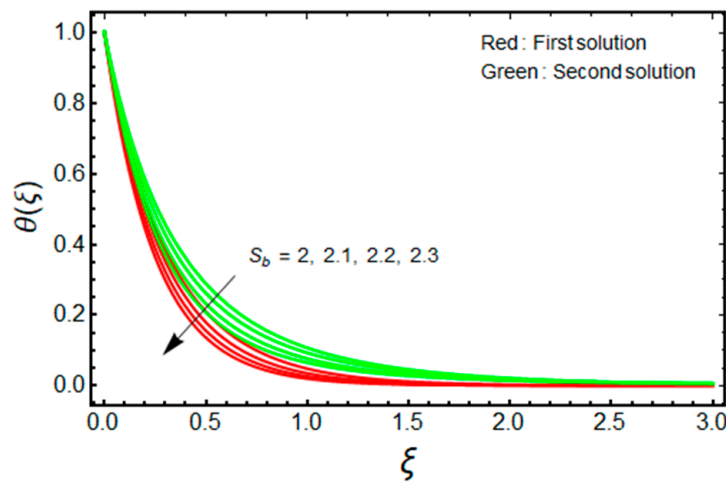

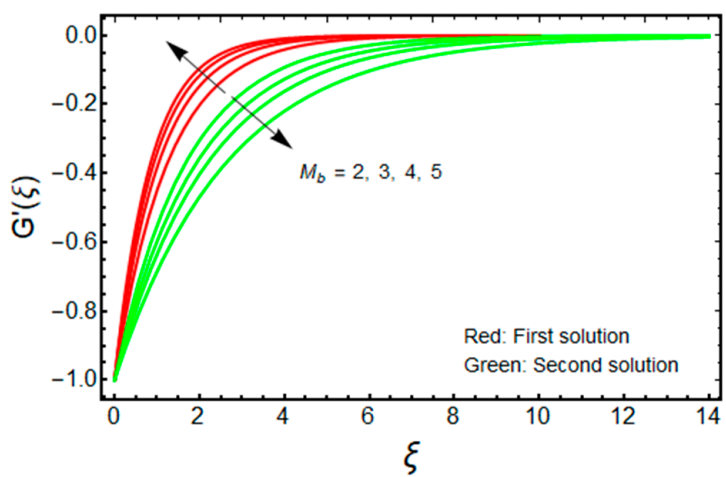**Figure 3.** Effect of S_b on $\theta(\xi)$ when $\phi = 0.025$, $\chi = 1$, $M_b = 0.5$, $R_d = 1.5$, $m = 1$.

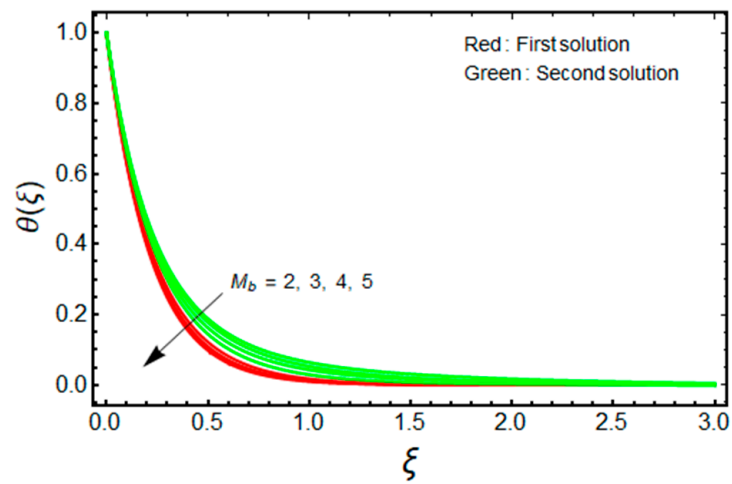**Figure 4.** Effect of M_b on $G'(\xi)$ when $\phi = 0.025$, $\chi = 1$, $S_b = 2.5$.

Figure 5. Effect of M_b on $\theta(\xi)$ when $\phi = 0.025$, $\chi = 1$, $S_b = 2.5$, $R_d = 1.5$, $m = 1$.
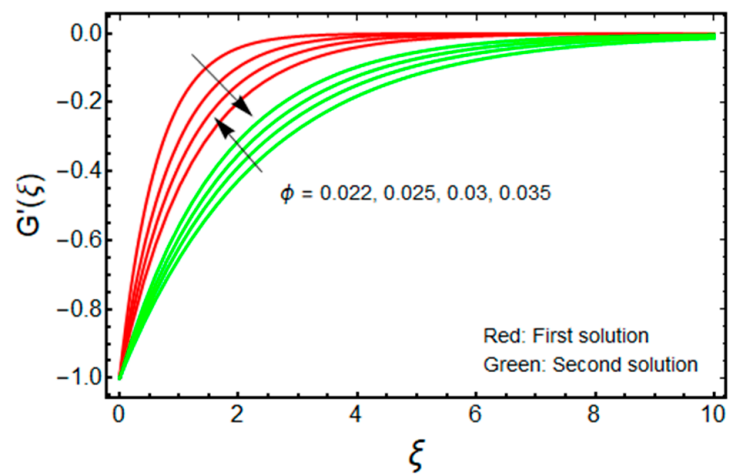

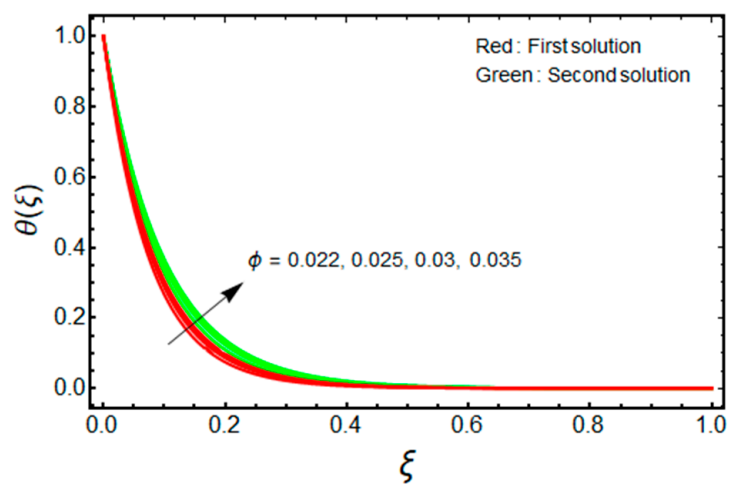**Figure 6.** Effect of ϕ on $G'(\xi)$ when $S_b = 2.5$, $\chi = 1$, $M_b = 0.5$.

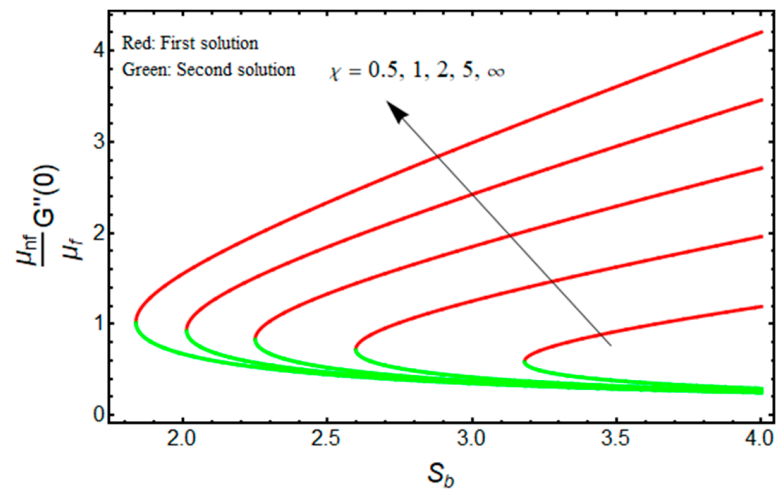**Figure 7.** Effect of ϕ on $\theta(\xi)$ when $S_b = 2.5$, $\chi = 1$, $M_b = 0.5$, $R_d = 1.5$, $m = 1$.

Figure 8. Effect of χ on $\left(\mu_{nf}/\mu_f\right)G''(0)$ versus S_b when $\phi = 0.025$, $M_b = 0.5$.
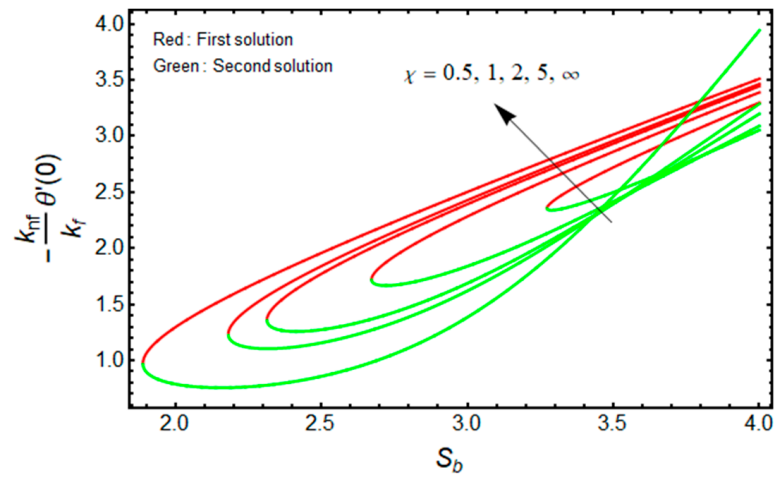

Figure 9. Effect of χ on $-\left(k_{nf}/k_f\right)\theta'(0)$ versus S_b when $\phi = 0.025$, $M_b = 0.5$, $R_d = 1.5$, $m = 1$.
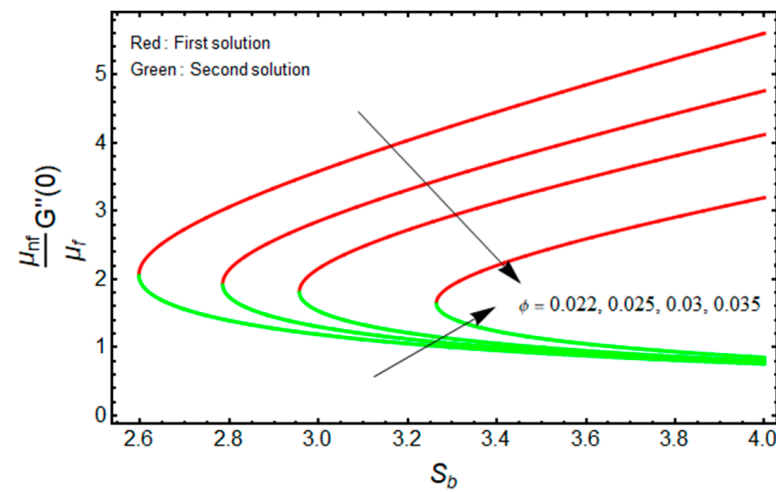

Figure 10. Effect of χ on $\left(\mu_{nf}/\mu_f\right)G''(0)$ versus S_b when $\chi = 1$, $M_b = 0.5$.
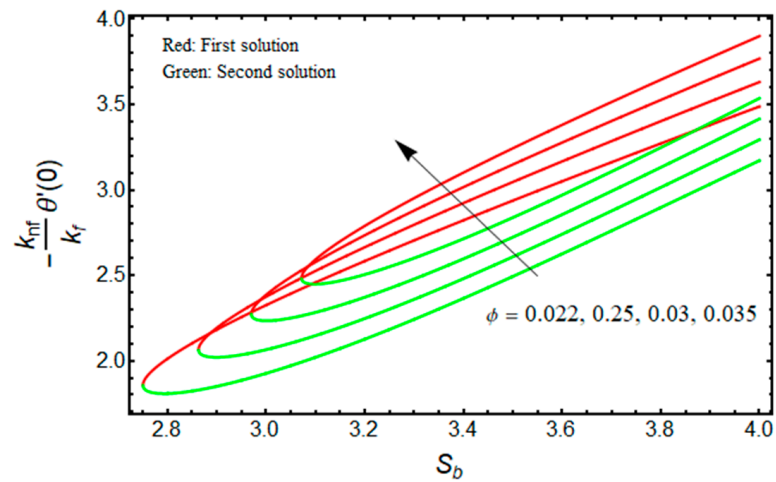
Figure 11. Effect of ϕ on $-\left(k_{nf}/k_f\right)\theta'(0)$ versus S_b when $\chi = 1$, $M_b = 0.5$, $R_d = 1.5$, $m = 1$.
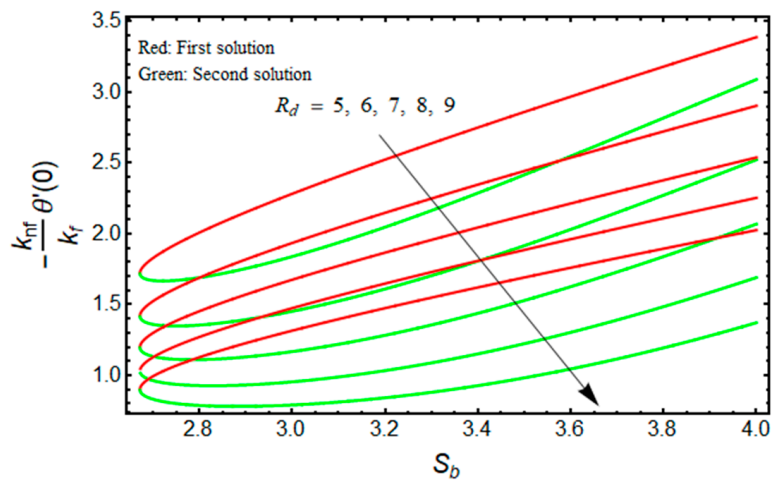

Figure 12. Effect of R_d on $-\left(k_{nf}/k_f\right)\theta'(0)$ versus S_b when $\phi = 0.025$, $\chi = 1$, $M_b = 0.5$, $m = 1$.

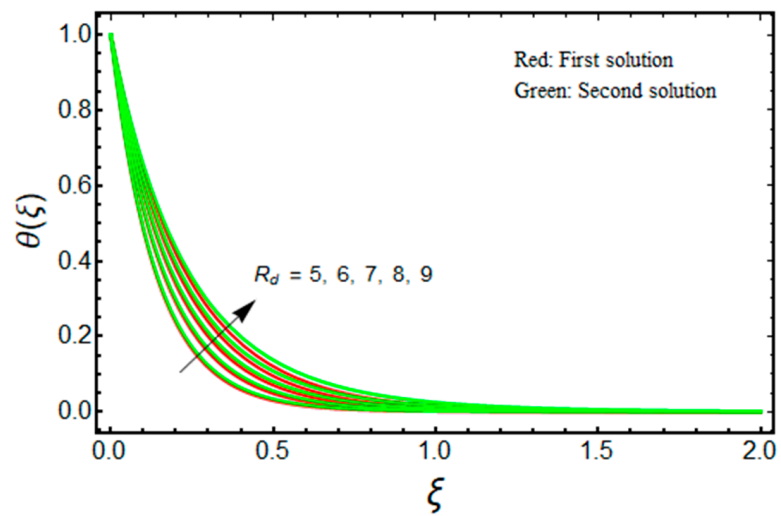**Figure 13.** Effect of R_d on $\theta(\xi)$ when $\phi = 0.025$, $\chi = 1$, $M_b = 0.5$, $m = 1$.

Table 3. Values of $\left(\mu_{nf}/\mu_f\right)G''(0)$ for distinct values of S_b, χ, ϕ, and M_b.

χ	M_b	ϕ	S_b	3.5	4	4.5	5
0.5	0.5	0.025	First solution	2.58605	3.40613	4.09306	4.73029
			Second solution	1.17470	0.89187	0.74219	0.64220
1	0.5	0.025	First solution	4.66415	5.63891	6.55804	7.44685
			Second solution	0.97697	0.80809	0.69483	0.61190
2	0.5	0.025	First solution	6.60110	7.81896	8.99505	10.14620
			Second solution	0.92040	0.77704	0.67544	0.59881
5	0.5	0.025	First solution	8.50938	9.98435	11.42330	12.83980
			Second solution	0.89249	0.76064	0.66483	0.59149
∞	0.5	0.025	First solution	10.4065	12.1435	13.8436	15.5307
			Second solution	0.87575	0.75048	0.65812	0.58680

Table 4. Values of $-\left(k_{nf}/k_f\right)\theta'(0)$ for distinct values of S_b, χ, ϕ, R_d, m, and M_b.

χ	M_b	ϕ	R_d	m	S_b	3.5	4	4.5	5
0.5	0.5	0.025	5	1	First solution	2.82016	3.52056	4.10507	4.66170
					Second solution	2.61293	3.32299	3.99296	4.68492
1	0.5	0.025	5	1	First solution	3.04693	3.63183	4.18821	4.72967
					Second solution	2.66077	3.44115	4.28216	5.18029
2	0.5	0.025	5	1	First solution	3.13405	3.69660	4.24086	4.77445
					Second solution	2.70750	3.72440	4.87577	6.24120
5	0.5	0.025	5	1	First solution	3.19054	3.74125	4.27820	4.80674
					Second solution	2.85264	4.31988	6.24757	9.17801
∞	0.5	0.025	5	1	First solution	3.23132	3.77438	4.30633	4.83129
					Second solution	3.18356	5.90969	11.6249	39.6040

Figures 2 and 3 are organized to show the impact of S_b on the velocity and temperature of the water-based aluminum oxide nanofluid for the two distinct branch solutions (first and second), respectively. The velocity upsurges with elevated values of S_b for the first branch solution, while the contrary impact is observed for the branch of the second solution. Additionally, it is noticed from Figure 2 that the velocity boundary layer thickness (BLT) shrinks for the first branch solution and improves for the branch of the second solution due to the larger values of S_b. Alternatively, the temperature field declines significantly in both branches of the solution with the enrich values of S_b. Therefore, the thermal BLT reduces with S_b for the first branch solution as well as for the second branch solution, which is graphically depicted in Figure 3. In addition, for the larger mass suction parameter temperature fields, overshoot is achieved merely in the branch of the second solution. About the physical observation, the stronger wall mass transfer parameter S_b reduces the wall drag force to avoid the separations of the BL. The conclusion is that the field of velocity augments for the branch of the first solution, which is physically stable. Additionally, BLT shrinks with this continuous enhancement in the velocity and wall mass transfer parameter.

The impact of M_b on the velocity and temperature of the water-based aluminum oxide nanofluid for the two distinct branch solutions (first and second) is portrayed in

Figures 4 and 5, respectively. It is noted that for improving the values of M_b, the fields of velocity magnitude and thermal (BLT) decrease in the branch of the first solution and become slightly thicker for the branch of the second solution. Moreover, the gap between the outcomes of the green curves is stronger and better when compared to the outcome of the red curves. Generally, the magnetic field powerfully distresses the nanoparticles; hence the magnitude of the velocity increases by increasing M_b, while the temperature profile is diminished.

The dimensionless velocity and temperature distribution for the first branch solution as well as for the second branch solution against ξ, with the significant impact of ϕ, is described in Figures 6 and 7, respectively. It is noticed that the profile of velocity at a point decreases with ϕ for the first solution, and the influence of ϕ changes for the branch of the second outcome. However, the temperature field upsurges with ϕ for the first solution, and the impact of ϕ is similar for the second branch solution. Moreover, for the increasing values of ϕ, the velocity BLT is increased for the second solution and is decreased for the branch of the first solution, while the thermal BLT is significantly improved in both solution branches. Physically, the effects of the nanoparticles can disperse some energy in the compact form of heat. Simultaneously, if the influence of the aluminum oxide nanoparticle increases significantly, this may cause more dissipation of energy in the form of heat which yields to enhance thermal conductivity. As a result, the temperature profile and the thermal BLT are augmented for the first and second solution branches.

The quantities of $\left(\mu_{nf}/\mu_f \right) G''(0)$ and $-\left(k_{nf}/k_f \right) \theta'(0)$ related to the friction factor (wall drag force) and heat transfer (wall temperature gradient) of the water-based aluminum oxide nanofluid for the first and second branch solutions versus S_b, owing to the effects of the Casson parameter χ, are graphically demonstrated in Figures 8 and 9, respectively. Outcomes recommend that the values of $\left(\mu_{nf}/\mu_f \right) G''(0)$ augments with the higher value of χ as well as the wall mass transfer parameter for the branch of the first solution, and it declines for the stronger Casson parameter χ for the branch of the second solution (see Figure 8) due to the elasticity of the fluid flow. Meanwhile, the wall temperature gradient $-\left(k_{nf}/k_f \right) \theta'(0)$ upsurges with χ for the branch of the first solution, but rises and falls in some specific portion of the domain (such as the wall mass transfer parameter) for the branch of the second solution (see Figure 9). In addition, the turning point of the existence of multiple solutions reduces with the larger values of M_b.

Figures 10 and 11 illustrate the significant impact of ϕ on $\left(\mu_{nf}/\mu_f \right) G''(0)$, and $-\left(k_{nf}/k_f \right) \theta'(0)$ against S_b for the double solution branches, respectively. From Figure 10, it is deeply noticed that for increasing S_b and ϕ, the friction factor is decreased for the branch of the first solution, and the impacts of ϕ and S_b are upturned for the branch of the second solution. However, the heat transfer rate is uplifting for both solution branches with a higher value of ϕ (see Figure 11). Additionally, the turning points of the existence of solutions upsurge with stronger values of ϕ. This is due to the fact that nanofluid improves the temperature field in the boundary layer. The finding also acknowledges the physical behavior, as increasing the volume of nanoparticles augments the thermal conductivity. The thermophysical properties have a direct impact on the effectiveness of nanofluids in thermal systems.

Figure 12 depicts the behavior of $-\left(k_{nf}/k_f \right) \theta'(0)$ for S_b as R_d varies. The lower and upper branch solutions indicate the value of $-\left(k_{nf}/k_f \right) \theta'(0)$ decelerates as R_d enhances. The stronger influence of radiation augments the nanofluid temperature inside the region of the boundary layer due to the fact that the conduction heat transport rate is augmented at the sheet surface. This fact is supported through the profile of temperature in Figure 13, where the nanofluid temperature uplifts when R_d enhances. As a result, thermal conductivity rises, resulting in a decline in the convective heat transfer rate.

5. Conclusions

In the current exploration, the impact of magnetic fields on the radiative flow induced by Al_2O_3 nanofluid past a radially shrinking sheet was investigated. In addition, the effectiveness of fluid flow, viscosity, and thermal conductivity were examined using the KKL model. Closed-form double solutions of leading transport equations were presented. The effects of relevant parameters on the explained flow are discussed with the assistance of graphs. The important results of the investigations are gathered as follows:

- The suction and magnetic parameters accelerate the velocity in the first branch solution and decelerate in the second branch solution, whilst declining the temperature distribution in both branch solutions.
- The temperature profile uplifts due to the solid nanoparticle volume fraction in both solutions, while the velocity increases and decreases due to the solid nanoparticle volume fraction in the first and second branch solutions, respectively.
- The heat transfer and the friction factor increase due to the Casson parameter.
- The nanoparticle volume fraction augments the heat transfer and declines the friction factor.

The current findings highlight the importance of the technology of heat exchangers, storage of geothermal storage, materials processing, and all other procedures inspired by the concept of heat development. The utilization of heat transfer fluids incorporating the dispersion of nanoparticles to resolve the problems of cooling in thermal systems is a significant technological application.

Nomenclature

$u_w(r_b)$	Velocity of the shrinking disk (m/s)
$B(r_b)$	Variable magnetic field strength (Tesla)
B_0	Constant magnetic field strength (Tesla)
$w_w(r_b)$	Wall mass transfer velocity (m/s)
$T_w(r_b)$	Wall temperature (K)
v_0, c	Arbitrary constants
T_∞	Ambient temperature (K)
T_b	Fluid temperature (K)
q_{rad}	Radiative heat flux
T_0	Constant reference temperature (K)
$G(\xi)$	Dimensionless velocity
M_b	Magnetic parameter
Pr	Prandtl number

S_b	Mass transfer factor
Nu_{r_b}	Heat transfer
C_g	Skin friction coefficient
Re_{r_b}	Reynolds number
D	Denotes the roots of the equation
$G(\xi)$	Dimensionless velocity
R_d	Radiation parameter
m	Relative factor of the power-law index
k_C	Mean absorption coefficient (1/m)
k	Thermal conductivity (W/(m·K))
u_b, w_b	Velocity components along the r_b- and z_b-axes (m/s)
(r_b, δ, z_b)	Cylindrical coordinates (m)
c_p	Specific heat at constant pressure (J/Kg·K)
B_1 and B_2	Arbitrary constants

Greek Symbols

ν_f	Kinematic viscosity (m^2/s)
γ and h	Empirical functions
$\theta(\xi)$	Dimensionless temperature
χ	Non-Newtonian or Casson fluid parameter
σ	Electrical conductivity (Ω^{-1}m^{-1})
μ	Dynamic viscosity (N·s/m^2)
ξ	Pseudo-similarity variable
ρ	Density (kg/m^3)
σ_C	Stefan-Boltzmann constant (W/(m^2·K^4))
ψ	Stream function
η	New similarity variable
ϕ	Solid nanoparticle volume fraction

Acronyms

KKL	Koo–Kleinstreuer–Li
MHD	Magnetohydrodynamics
EOF	Electro-osmotic forces
Al$_2$O$_3$	Alumina
2D, 3D	Two and three-dimensional
BCs	Boundary conditions
BLT	Boundary layer thickness
BLF	Boundary layer flow
VD	Viscous dissipation
TIR	Thermal interfacial resistance

Subscripts

pa	Nanoparticles
nf	Nanofluid
f	Regular based-fluid
w	Wall boundary condition
∞	Far-field condition

Superscript

$'$	Derivative with respect to ξ

Appendix A

The magnetic term in the balance of momentum (Equation (3)) is explained here. In the given paper, the magnetic body force, **F**, is defined by:

$$\mathbf{F} = \mathbf{J} \times \mathbf{B}$$

with the electric current vector, **J**:

$$\mathbf{J} = \sigma_{nf}(\mathbf{E} + \mathbf{V} \times \mathbf{B})$$

where σ_{nf} is the electrical conductivity of the nanofluid and **E** is the electric field vector. It is assumed that the imposed magnetic field, $\mathbf{B} = \langle 0, 0, r_b B_0 \rangle$, acts in the z_b−direction, which is normal for the disk where the boundary layer is formed; the flow is confined to $z_b > 0$. Based on the flow assumption due to a low Reynolds number, the induced magnetic field can be neglected. Moreover, the electric field vector, **E**, is assumed to be zero, i.e., the electric and polarization effects are neglected. Therefore,

$$\mathbf{J} = \sigma_{nf}(\mathbf{V} \times \mathbf{B}) = \sigma_{nf}[\langle u_b, v_b, w_b \rangle \times \langle 0, 0, r_b B_0 \rangle]$$

$$= \sigma_{nf} \begin{vmatrix} \mathbf{i} & \mathbf{j} & \mathbf{k} \\ u_b & v_b & w_b \\ 0 & 0 & r_b B_0 \end{vmatrix}$$

$$= \sigma_{nf} \langle v_b r_b B_0, -u_b r_b B_0, 0 \rangle$$

where u_b, v_b, and w_b are the velocity components in the r_b, δ, and z_b directions, respectively. Further, here in the considered problem, the velocity field, **V**, is assumed as $\mathbf{V} = \langle u_b, 0, 0 \rangle$. Putting this in the above Equation (3), we get

$$\mathbf{J} = \sigma_{nf}(\mathbf{V} \times \mathbf{B}) = \sigma_{nf} \langle 0, -u_b r_b B_0, 0 \rangle$$

Then, the expression $\mathbf{J} \times \mathbf{B}$ can be written as:

$$\mathbf{J} \times \mathbf{B} = \sigma_{nf}[\langle 0, -u_b r_b B_0, 0 \rangle \times \langle 0, 0, r_b B_0 \rangle],$$

$$= \sigma_{nf} \begin{vmatrix} \mathbf{i} & \mathbf{j} & \mathbf{k} \\ 0 & -u_b r_b B_0 & 0 \\ 0 & 0 & r_b B_0 \end{vmatrix},$$

$$= \sigma_{nf} \langle -u_b r_b{}^2 B_0{}^2, 0, 0 \rangle.$$

Thus,

$$(\mathbf{J} \times \mathbf{B})_{r_b} = -\sigma_{nf} r_b{}^2 B_0{}^2 u_b, \quad (\mathbf{J} \times \mathbf{B})_\delta = 0, \quad \text{and} \quad (\mathbf{J} \times \mathbf{B})_{z_b} = 0,$$

where $(\mathbf{J} \times \mathbf{B})_{r_b}$, $(\mathbf{J} \times \mathbf{B})_\delta$, and $(\mathbf{J} \times \mathbf{B})_{z_b}$ are the components of $\mathbf{J} \times \mathbf{B}$ in the r_b, δ, and z_b directions, respectively. In addition, the expression of the electrical conductivity σ_{nf} depends on ϕ.

References

1. Choi, S.U.S. Enhancing thermal conductivity of fluids with nanoparticles. *ASME Int. Mech. Eng.* **1995**, *66*, 99–105.
2. Hamad, M.A.; Pop, I. Scaling transformations for boundary layer flow near the stagnation-point on a heated permeable stretching surface in a porous medium saturated with a nanofluid and heat generation/absorption effects. *Transp. Porous Med.* **2010**, *87*, 25–39. [CrossRef]
3. Makinde, O.D.; Aziz, A. Boundary layer flow of a nanofluid past a stretching sheet with a convective boundary condition. *Int. J. Therm. Sci.* **2011**, *50*, 1326–1332. [CrossRef]
4. Rana, P.; Bhargava, R. Flow and heat transfer of a nanofluid over a nonlinearly stretching sheet: A numerical study. *Commun. Nonlinear Sci. Numer. Simul.* **2012**, *17*, 212–226. [CrossRef]

5. Pal, D.; Mandal, G. Mixed convection-radiation on stagnation-point flow of nanofluids over a stretching/shrinking sheet in a porous medium with heat generation and viscous dissipation. *J. Petrol. Sci. Eng.* **2015**, *126*, 16–25. [CrossRef]
6. Hayat, T.; Khan, M.I.; Farooq, M.; Yasmeen, T.; Alsaedi, A. Water-carbon nanofluid flow with variable heat flux by a thin needle. *J. Mol. Liq.* **2016**, *224*, 786–791. [CrossRef]
7. Eid, M.R. Chemical reaction effect on MHD boundary layer flow of two-phase nanofluid model over an exponentially stretching sheet with a heat generation. *J. Mol. Liq.* **2016**, *220*, 718–725. [CrossRef]
8. Zaib, A.; Rashidi, M.M.; Chamkha, A.J. Flow of nanofluid containing gyrotactic microorganisms over static wedge in Darcy–brinkman porous medium with convective boundary condition. *J. Porous Med.* **2018**, *21*, 911–928. [CrossRef]
9. Soomro, F.A.; Zaib, A.; Haq, R.U.; Sheikholeslami, M. Dual nature solution of water functionalized copper nanoparticles along a permeable shrinking cylinder: FDM approach. *Int. J. Heat Mass Transf.* **2019**, *129*, 1242–1249. [CrossRef]
10. Khan, U.; Shafiq, A.; Zaib, A.; Baleanu, D. Hybrid nanofluid on mixed convective radiative flow from an irregular variably thick moving surface with convex and concave effects. *Case Stud. Therm. Eng.* **2020**, *21*, 100660. [CrossRef]
11. Zaher, A.Z.; Ali, K.K.; Mekheimer, K.S. Electroosmosis forces EOF driven boundary layer flow for a non-Newtonian fluid with planktonic microorganism: Darcy Forchheimer model. *Int. J. Num. Meth. Heat Fluid Flow* **2021**, *31*, 2534–2559. [CrossRef]
12. Gowda, R.J.P.; Kumar, R.N.; Prasannakumara, B.C.; Nagaraja, B.; Gireesha, B.J. Exploring magnetic dipole contribution on ferromagnetic nanofluid flow over a stretching sheet: An application of Stefan blowing. *J. Mol. Liq.* **2021**, *335*, 116215. [CrossRef]
13. Shahid, A.; Bhatti, M.M.; Ellahi, R.; Mekheimer, K.S. Numerical experiment to examine activation energy and bi-convection Carreau nanofluid flow on an upper paraboloid porous surface: Application in solar energy. *Sustain. Energy Technol. Assess.* **2022**, *52*, 102029. [CrossRef]
14. Mukhopaday, S. Casson fluid flow and heat transfer over a nonlinearly stretching surface. *Chin. Phys. B* **2013**, *22*, 074701. [CrossRef]
15. Nadeem, S.; Haq, R.U.; Lee, C. MHD flow of a Casson fluid over an exponentially shrinking sheet. *Sci. Iran.* **2012**, *19*, 1550–1553. [CrossRef]
16. Pramanik, S. Casson fluid flow and heat transfer past an exponentially porous stretching surface in presence of thermal radiation. *Ain Shams Eng. J.* **2013**, *1*, 205–212. [CrossRef]
17. Haq, R.U.; Nadeem, S.; Khan, Z.H.; Okedayo, T.G. Convective heat transfer and MHD effects on Casson nanofluid flow over a shrinking sheet. *Cent. Eur. J. Phys.* **2014**, *12*, 862–871. [CrossRef]
18. Makinde, O.D.; Sandeep, N.; Ajayi, T.M.; Animasaun, I.L. Numerical exploration of heat transfer and Lorentz force effects on the flow of MHD Casson fluid over an upper horizontal surface of a thermally stratified melting surface of a paraboloid of revolution. *Int. J. Nonlinear Sci. Numer. Simul.* **2018**, *19*, 93–106. [CrossRef]
19. Faraz, F.; Imran, S.M.; Ali, B.; Haider, S. Thermo-Diffusion and multi-slip effect on anaxisymmetric Casson flow over a unsteady radially stretching sheet in the presence of chemical reaction. *Processes* **2019**, *7*, 851. [CrossRef]
20. Khan, U.; Bilal, S.; Zaib, A.; Makinde, O.D.; Wakif, A. Numerical simulation of a nonlinear coupled differential system describing a convective flow of Casson gold–blood nanofluid through a stretched rotating rigid disk in the presence of Lorentz forces and nonlinear thermal radiation. *Numer. Methods Partial Diff. Eq.* **2022**, *38*, 308–328. [CrossRef]
21. Zaib, A.; Haq, R.U.; Chamkha, A.J. Mixed convective flow of a Casson fluid over a vertical plate in Darcy–Brinkman porous medium with slips. *J. Porous Med.* **2021**, *24*, 1–12. [CrossRef]
22. Jyothi, A.M.; Kumar, R.N.; Gowda, R.J.P.; Veeranna, Y.; Prasannakumara, B.C. Impact of activation energy and gyrotactic microorganisms on flow of Casson hybrid nanofluid over a rotating moving disk. *Heat Transf.* **2021**, *96*, 075210. [CrossRef]
23. Hossain, M.A.; Takhar, H.S. Radiation effect on mixed convection along a vertical plate with uniform surface temperature. *Int. J. Heat Mass Transf.* **1996**, *31*, 243–248. [CrossRef]
24. Takhar, H.S.; Gorla, R.S.R.; Soundalgekar, V.M. Radiation effects on MHD free convection flow of a gas past a semi-infinite vertical plate. *Int. J. Numer. Methods Heat Fluid Flow* **1996**, *6*, 77–83. [CrossRef]
25. Hossain, M.A.; Alim, M.A.; Rees, D.A. The effect of radiation on free convection from a porous vertical plate. *Int. J. Heat Mass Transf.* **1999**, *42*, 181–191. [CrossRef]
26. Hayat, T.; Qasim, M. Radiation and magnetic field effects on the unsteady mixed convection flow of a second grade fluid over a vertical stretching sheet. *Int. J. Numer. Methods Fluids* **2011**, *66*, 820–832. [CrossRef]
27. Mukhopadhyay, S.; Bhattacharyya, K.; Layek, G.C. Steady boundary layer flow and heat transfer over a porous moving plate in presence of thermal radiation. *Int. J. Heat Mass Transf.* **2011**, *54*, 2751–2757. [CrossRef]
28. Daniel, Y.S.; Aziz, Z.A.; Ismail, Z.; Shah, F. Thermal radiation on unsteady electrical MHD flow of nanofluid over stretching sheet with chemical reaction. *J. King Saud Univ. Sci.* **2019**, *31*, 804–812. [CrossRef]
29. Mekheimer, K.S.; Ramadan, S.F. New Insight into gyrotactic microorganisms for Bio-thermal convection of Prandtl nanofluid past a stretching/shrinking permeable sheet. *SN Appl. Sci.* **2020**, *2*, 450. [CrossRef]
30. Ramana, R.M.; Kumar, J.G.; Raju, K.V. Melting and radiation effects on MHD heat and mass transfer of Casson fluid flow past a permeable stretching sheet in the presence of chemical reaction. *AIP Proced.* **2020**, *2246*, 020021.
31. Abbas, W.; Mekheimer, K.S.; Ghazy, M.M.; Moawad, A.M.A. Thermal radiation effects on oscillatory squeeze flow with a particle-fluid suspension. *Heat Transf.* **2021**, *50*, 2129–2149. [CrossRef]
32. Khan, U.; Zaib, A.; Khan, I.; Nisar, K.S. Insight into the dynamics of transient blood conveying gold nanoparticles when entropy generation and Lorentz force are significant. *Int. Commun. Heat Mass Transf.* **2021**, *127*, 105415. [CrossRef]

33. Ariel, P.D. Axisymmetric flow due to a stretching sheet with partial slip. *Comput. Math. Appl.* **2007**, *54*, 1169–1183. [CrossRef]

34. Mirgolbabaei, H.; Ganji, D.D.; Etghani, M.M.E.; Sobati, A. Adapted variational iteration method and axisymmetric flow over a stretching sheet. *Wolrd J. Model. Simul.* **2009**, *5*, 307–314.

35. Ariel, P.D. Axisymmetric flow of a second grade fluid past a stretching sheet. *Int. J. Eng. Sci.* **2001**, *39*, 529–553. [CrossRef]

36. Sahoo, B. Effects of partial slip on axisymmetric flow of an electrically conducting viscoelastic fluid past a stretching sheet. *Central Eur. J. Phys.* **2010**, *8*, 498–508. [CrossRef]

37. Shahzad, A.; Ali, R.; Kamran, M.; Khan, S.U.D.; Khan, S.U.; Farooq, A. Axisymmetric flow with heat transfer over exponentiallystretching sheet: A computational approach. *Phys. A* **2020**, *554*, 124242. [CrossRef]

38. Mukhopadhyay, S. Effects of thermal radiation on Casson fluid flow and heat transfer over an unsteady stretching surface subjected to suction/blowing. *Chin. Phys. B* **2013**, *22*, 114702. [CrossRef]

39. Mondal, S.; Sibanda, P. Unsteady Casson nanofluid flow over a stretching sheet with thermal radiation, convective and slip boundary conditions. *Alex. Eng. J. Eng.* **2016**, *55*, 1025–1035.

40. Azeem, S.; Ramzan, A.; Masood, K. On the exact solution for axisymmetric flow and heat transfer over a nonlinear radially stretching sheet. *Chin. Phys. Lett.* **2012**, *29*, 084705.

41. Khan, U.; Zaib, A.; Khan, I.; Nisar, K.S. Activation energy on MHD flow of titanium alloy (Ti_6Al_4V) nanoparticle along with a cross flow and streamwise direction with binary chemical reaction and non-linear radiation: Dual Solutions. *J. Mater. Res. Technol.* **2020**, *9*, 188–199. [CrossRef]

42. Alghamdi, M.; Wakif, A.; Thumma, T.; Khan, U.; Baleanu, D.; Rasool, G. Significance of variability in magnetic field strength and heat source on the radiative-convective motion of sodium alginate-based nanofluid within a Darcy–Brinkman porous structure bounded vertically by an irregular slender surface. *Case Stud. Therm. Eng.* **2021**, *28*, 101428. [CrossRef]

43. Koo, J.; Kleinstreuer, C. Viscous dissipation effects in microtubes and microchannels. *Int. J. Heat Mass Transf.* **2004**, *47*, 3159–3169. [CrossRef]

44. Koo, J. Computational Nanofluid Flow and Heat Transfer Analyses Applied to Micro-Systems. Ph.D. Thesis, NC State University, Raleigh, NC, USA, 2005.

45. Jang, S.P.; Choi, S.U. Role of Brownian motion in the enhanced thermal conductivity of nanofluids. *Appl. Phys. Lett.* **2004**, *84*, 4316–4318. [CrossRef]

46. Prasher, R.; Bhattacharya, P.; Phelan, P.E. Thermal conductivity of nanoscale colloidal solutions (nanofluids). *Phys. Rev. Lett.* **2005**, *94*, 025901. [CrossRef]

47. Li, J. Computational Analysis of Nanofluid Flow in Microchannels with Applications to Micro-Heat Sinks and Bio-MEMS. Ph.D. Thesis, University Libraries, North Carolina State University, Raleigh, NC, USA, 2008.

48. Fang, T.; Yao, S.; Zhang, J.; Aziz, A. Viscous flow over a shrinking sheet with a second order slip flow model. *Commun. Nonlinear Sci. Num. Simul.* **2010**, *15*, 1831–1842. [CrossRef]

49. Nandeppanavar, M.M.; Vajravelu, K.; Abel, M.S.; Siddalingappa, M.N. Second order slip flow and heat transfer over astretching sheet with non-linear Navier boundary condition. *Int. J. Therm. Sci.* **2012**, *58*, 143–150. [CrossRef]

50. Turkyilmazoglu, M. Heat and mass transfer of MHD second order slip flow. *Comp. Fluids* **2013**, *71*, 426–434. [CrossRef]

51. Hakeem, A.K.A.; Ganesh, N.V.; Ganga, B. Magnetic field effect on second order slip flow of nanofluid over a stretching/shrinking sheet with thermal radiation effect. *J. Magn. Magn. Mat.* **2015**, *381*, 243–257. [CrossRef]